Supplementary Information

Ultra-compact nonvolatile phase shifter based on electrically reprogrammable transparent phase change materials

Carlos Ríos[1,2,†,*], Qingyang Du[3,†,*], Yifei Zhang[4], Cosmin-Constantin Popescu[4], Mikhail Y. Shalaginov[4], Paul Miller[5], Christopher Roberts[5], Myungkoo Kang[6], Kathleen A. Richardson[6,7], Tian Gu[4,8], Steven A. Vitale[5,*], Juejun Hu[4,8]

[1]Department of Materials Science & Engineering, University of Maryland, College Park, MD, USA
[2]Institute for Research in Electronics and Applied Physics, University of Maryland, College Park, MD, USA
[3]Research Center for Intelligent Optoelectronic Computing, Zhejiang Lab, Hangzhou, China, 311121
[4]Department of Materials Science & Engineering, Massachusetts Institute of Technology, Cambridge, MA, USA
[5]Lincoln Laboratory, Massachusetts Institute of Technology. Lexington, MA, USA
[6]CREOL, The College of Optics & Photonics, University of Central Florida, Orlando, FL USA
[7]Department of Materials Science and Engineering, University of Central Florida, Orlando, FL USA
[8]Materials Research Laboratory, Massachusetts Institute of Technology, Cambridge, MA, USA

[†]These authors contributed equally
**riosc@umd.edu, qydu@zhejianglab.edu.cn, steven.vitale@ll.mit.edu*

This document contains the following supplementary sections.

S1. Fabrication

S2. Electrical design and characterization of doped-silicon microheaters

S3. Thermo-optic (volatile) characterization in 2×2 optical switch

S4. Time-domain measurements

S5. Propagation loss due to Sb_2Se_3 and doped-silicon

S6. Scattering losses analysis

S7. Extinction ratio modulation in add-drop ring resonators

S8. Other results for MZI modulators

S9. SEM images for devices after switching

S10. References

S1. Fabrication

The fabrication process was carried out in two parts, as described in the Methods section of the main paper. The first process comprised the fabrication of the microheaters using a combination of photolithography, ion implantation, and metallization using the 90-nm CMOS line at Lincoln Laboratory 200 nm wafer foundry. We used 220nm-thick silicon-on-insulator wafers and carried out all the fabrication steps shown in Fig. S1. The second part of the process, which was carried out in MIT.nano, was dedicated to patterning the waveguides (half-etched ridge waveguides) via electron beam lithography and etching, the deposition of Sb_2Se_3 followed by lift-off patterning, and capping with alumina using atomic layer deposition (ALD). A full sketch of the fabrication process is shown in Fig. S2.

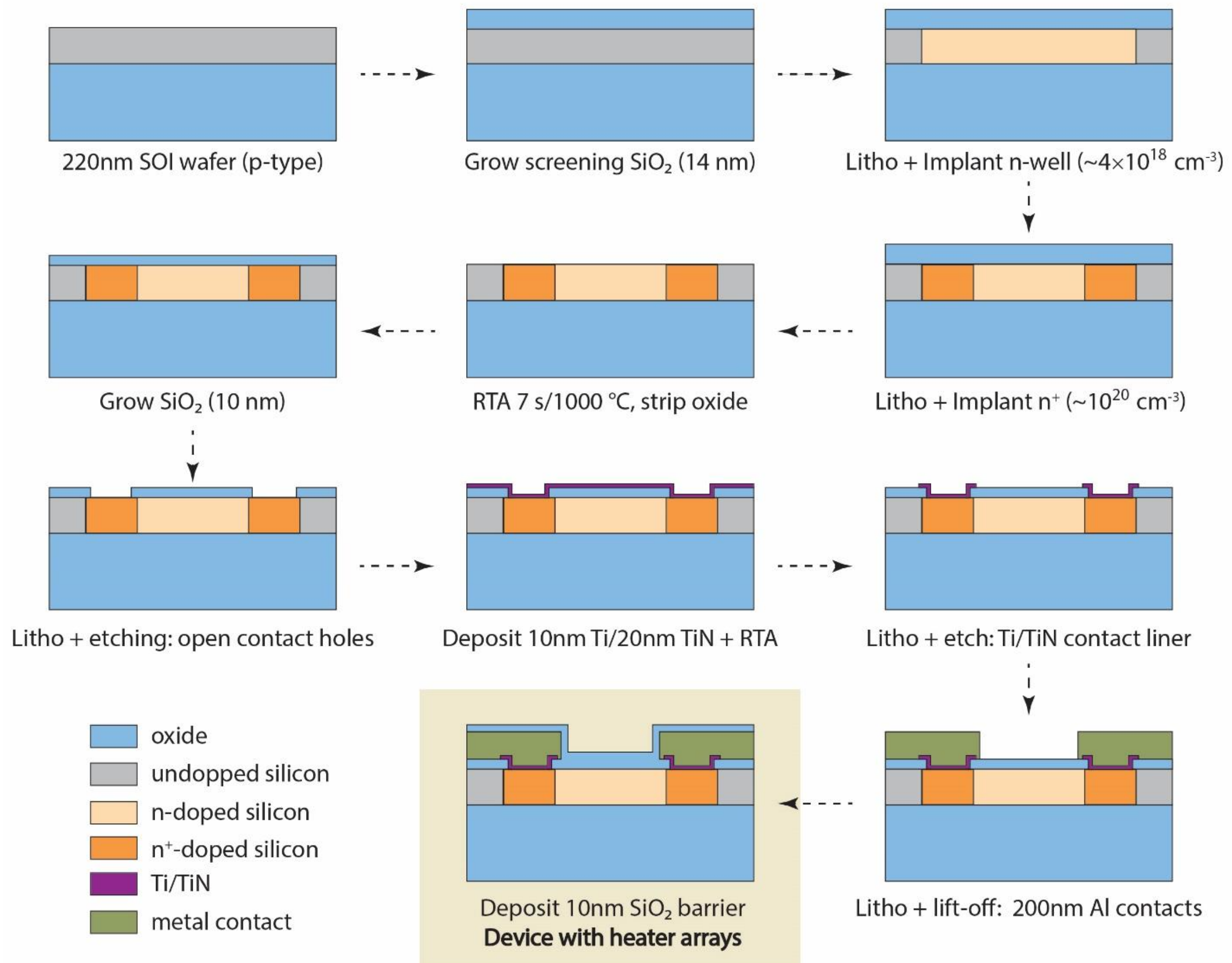

Figure S1. Fabrication steps to define doped-silicon microheater arrays.

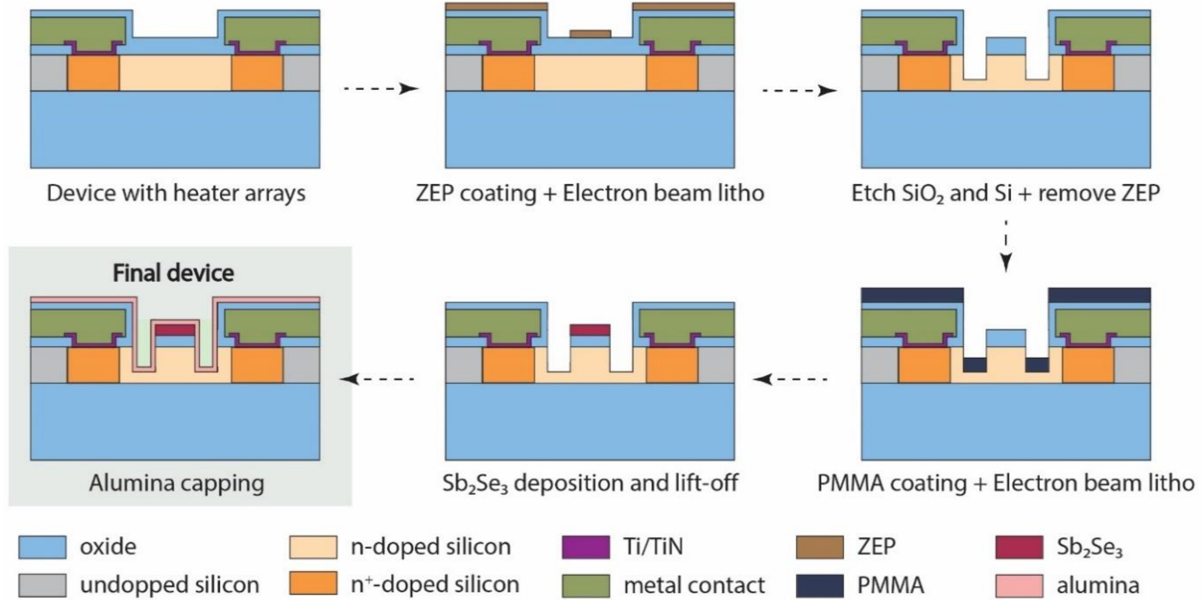

Figure S2. Fabrication steps for backend integration of Sb_2Se_3 with microheaters

S2. Electrical design and characterization of doped-silicon microheaters

Three key metrics of the heater were considered in the design process: speed, energy consumption, and optical losses. Amorphization of Sb_2Se_3 involves heating the material above its melting point (T_m ~ 610 °C) and rapidly quenching down to "freeze" the liquid-like amorphous structure. The amorphization process can, in principle, be arbitrarily fast, although, in practice, it is limited by the heat dissipation rate of the microheater. To crystallize Sb_2Se_3, the material is heated to above its crystallization temperature (T_x = 200 °C) and held until the transition is complete. In our experimental demonstrations, Sb_2Se_3 requires up to one millisecond to fully crystallize; however, we found that pulses down to even 5 μs were enough to induce partial crystallization. Due to the longer duration of the crystallization process, the heater energy consumption is predominantly dictated by the time it takes to recrystallize fully. In contrast, the peak power requirements are dictated by the energy needed to heat the entire Sb_2Se_3 volume above the melting point. A compact phase shifter design and hence a small thermal mass are critical to minimizing the energy consumption. The driving voltage V is related to the energy consumption by $E = \frac{V^2}{R}\Delta t$, where R denotes the heater's electrical resistance and Δt is the electrical pulse duration. Therefore, the voltage can be tuned by adjusting the doping profile, the doping concentration, and electrical pulse width. Based on these general considerations, the microheater design was optimized under the following boundary conditions:

1) Dopant diffusion: diffusion induces doping profile change over heating cycles and causes undesired performance drift. Given that $T_m >> T_c$ and that diffusivity follows the exponential Arrhenius law, we only need to account for diffusion during the amorphization process. Consider a heating temperature of 700 °C, which is considerably higher than T_m with sufficient margin. The diffusivity of phosphorus

dopant in Si is $D_p = 5 \times 10^{-19}$ cm^2/s at 700 °C[1]. For 10^9 switching cycles and 10 µs maximum dwell time each cycle, the cumulative heating time $t_D = 10^4$ s. We can then estimate the diffusion distance to be $\sqrt{2D_P t_D}$ = 1 nm, far smaller than the linear dimensions of the heater. For crystallization at 200°C $D_p \sim 10^{-25}$ cm^2/s which , even if considering the $t_D = 10^7$ s due to 1 ms crystallization events, leads to a negligible diffusion distance since $\sqrt{2D_P t_D}$ = 0.01 nm. Because of these results, not further considerations were required in our design.

2) Free carrier absorption (FCA) vs. resistivity: high doping concentration reduces the resistance R and the driving voltage of the microheaters, while it increases the driving current. Low driving voltages are desirable because the goal is to achieve CMOS-compatible voltages (i.e., under 5V). Additionally, low voltage/high currents high-speed pulse generators are more common than high voltage/ low current ones. Considering the currents used in our approach: 3 mA – 8 mA vs. the voltages 3V- 20V, it would be trivial to double the current and having half of the voltages, while the opposite is more difficult from an instrumentation point of view. However, achieving lower voltages with high doping concentration has to be traded off with FCA. To optimize this trade-off, we introduced a two-step doping profile to lower the total resistance with minimal FCA penalty (Fig. 1a): the n^+ regions connect the heater to metal contacts with low resistance, while the lightly doped n central region (10 µm in total) defines the heating zone, which includes the waveguide. We followed the example of previous demonstrations of highly efficient thermo-optic phase shifters in the silicon-on-insulator (SOI) platform.[2] After testing four different doping combinations, we found a good balance with a concentration of $n \sim 4 \times 10^{18}$ cm^{-3}, which corresponds to a theoretical insertion loss of ~ 0.01 dB/µm due to FCA. We measured the total resistance and the I-V curves for each of the devices considered in this study, shown in Fig. S3a. Using the results in Fig. S3b we calculated the resistivity of our doped-silicon microheaters, since, from the fitting, we have:

$$R_T = R_C + \rho \frac{L}{tW} = R_C + \frac{A}{W} = (51.2 \pm 38.6)\Omega + \frac{(9886 \pm 149)\ \Omega\ \mu m^{-1}}{W}, \quad (1)$$

where R_c is the contact resistance, ρ is the resistivity, L the separation between both heaters, t the thickness, W the width of the heater (waist of the bow-tie as shown in Fig. S3a), and $A = \rho \frac{L}{t} = (9886 \pm 149)\ \Omega\ \mu m$. Considering our case, in which $L = 9.5\ \mu m$ with $t = 0.11\ \mu m$ for the slabs, and $L = 0.5\ \mu m$ with $t = 0.22\ \mu m$ for the waveguide, we found $\rho = 0.0108\ \Omega\ cm^{-1}$, which effectively corresponds to a doping concentration of $\sim 4 \times 10^{18}$ cm^{-3}, consistent with our ion implantation dose. Fig. S3c shows the I-V curves with a saturation effect due to the carrier mobility dependence on temperature, which is proportional to V. This saturation is responsible for the high voltage operation required to melt Sb_2Se_3 and trigger amorphization.

While our approach with light *n*-doping led to low losses, there is still plenty of room for improvement. Losses can be further suppressed by optimizing the size and doping concentration. In particular, the *n*-doping region length *L,* which in our experiments was fixed to 10 µm, can be further decreased without affecting the propagating mode due to the proximity of the n^+ regions. Our simulations show that n^+ regions close to 1 µm (i.e. *L*=*2* µm) to the waveguide do not affect the propagating mode. With a smaller *n*-doping region length (smaller *L*) in Eq. (1), the concentration of dopants can be decreased (higher ρ) while keeping the same total resistance, i.e., power consumption, with the benefit of diminishing the optical loss. Alternatively, more than two doping levels can be used, which is the norm for state-of-the-art foundry processed silicon photonic devices.

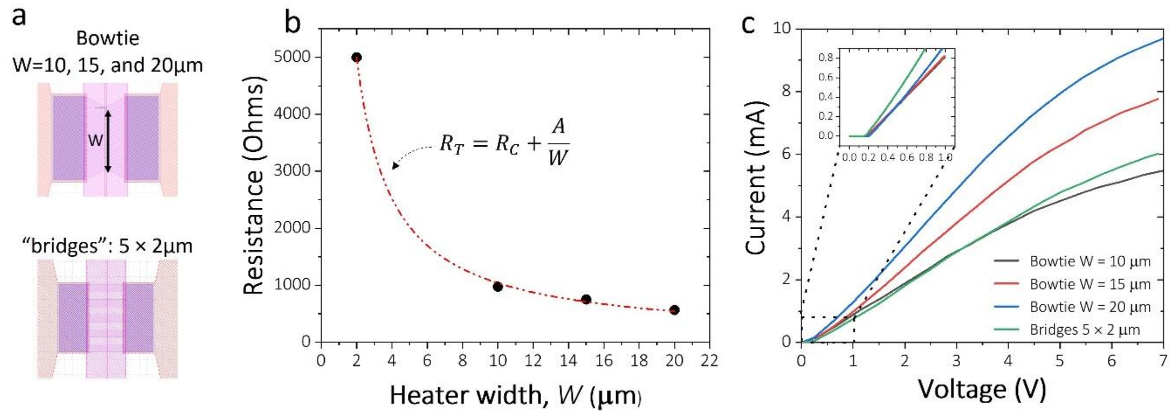

Figure S3. Electrical characterization of the devices shown in **a. b** Total resistance for four different devices shown in **a.** The red line is the fitting following the total resistance equation**.** From the fitting, we found $R_c = (51.2 \pm 38.6)\ \Omega$ and $A = (9886 \pm 149)\ \Omega \cdot \mu m$. **c** IV curves for the four different devices.

3) Heat localization: heat localization enhances spatial overlap between the optical mode and the heating zone to diminish the thermal mass and dictates the minimum distance between two consecutive microheaters (phase shifters). Thermal localization was achieved by combining two-step doping (which delimits heat generation in the lateral direction) and a bowtie-shaped or 'bridges'-shaped doped region (which confines the heat zone to a short longitudinal section of the waveguide). Using doping concentration modulation instead of Si etching to define the heating zone also eliminates optical scattering loss at patterned junctions and etched sidewalls. The heat localization in the devices we have studied was simulated and is shown in Fig. 1e and Fig. 5a of the main text. To avoid any thermal crosstalk during the switching event, devices should be at least 10µm apart, which still results in a small footprint. However, Sb_2Se_3 cells can be even closer if the transient response is not relevant and as long as the temperature in the neighbor heater does not result in phase transitions.

4) Thermal constant: the thermal constant of the microheater limits the speed at which a PCM cell is quenched, which in turn determines whether it amorphizes or recrystallizes after melting. While a long pulse might be used to elevate the temperature of Sb_2Se_3 above its melting point – as done for

$Ge_2Sb_2Se_4Te_1$ with a voltage pulse as low as 5 V [3] – the fast crystallization kinetics requires quenching times in the order of hundreds of nanoseconds. To achieve this, we took advantage of the good thermal conductivity of silicon itself. Using rib waveguides everywhere (or at least in the vicinity of the microheater), the silicon slab, together with the substrate, accelerates the heat dissipation process and allows us to achieve amorphization with a 400 ns-long pulse and a five ns trailing edge. The transient response of temperature for this pulse is shown in Fig. S4a, where quenching of ~400 ns led to amorphization. Having a high thermal conductive material surrounding the microheater also comes with the drawback of slower heating up, which is why we could not achieve amorphization under 400 ns without significantly increasing the voltage. For the 10 µm-long bow-tie microheater, we found that the maximum pulse length to trigger partial amorphization was 1 µs at 16.1 V [8.2 V], while for the 'bridges' devices, 1.05 µs at 21.1 V [10.8 V] triggered a full amorphization. Undercutting the oxide substrate and using suspended waveguides could be a strategy for fast heating up while keeping similar or lower voltages. A caveat is a longer thermal time constant; however, if using shorter pulses, 200 ns, for instance, a fast < 400 ns quenching is achievable even when the thermal time constant doubles its value.

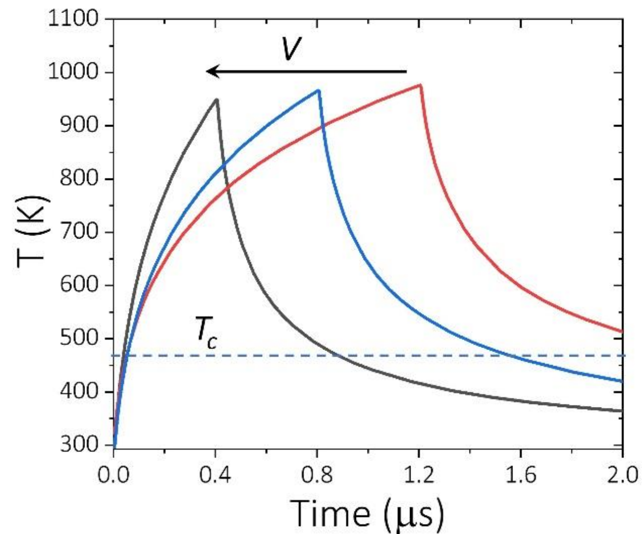

Figure S4. Simulation results for pulse excitation with varying voltage and the pulse width to achieve the melting temperature of 6 µm-long Sb_2Se_3 using a 10 µm-long bow-tie microheater (see Fig. 1a). A double exponential fitting of the cooling times led to fast and slow thermal constants $\tau_1 = 64$ ns and $\tau_2 = 450$ ns. Cooling down under the crystallization temperature was estimated to be approximately double the time of the pulse excitation.

S3. Thermo-optic (volatile) characterization of 2 × 2 optical switch

Applying a DC voltage to doped-silicon microheaters results in a thermo-optical effect that modulates the refractive index of silicon – a well-known effect used for volatile phase modulation in photonic integrated circuits.[2] While in this work we have used the microheater for transient heat stimuli to switch the Sb_2Se_3, our device can also be used for volatile phase modulation using said thermo-optical effect. An example of volatile modulation is shown in Fig. S5, where the transmission of an MZI switch is measured at 1550 nm while sweeping between 0-6 V during 2 s in each arm's microheater. Fig. S5 also corresponds to the MZI switch tested in Fig. 2d (main paper) and shows that both Sb_2Se_3 introduced the expected $\pi/2$ phase shift, while the different extinction ratio is due to the unbalanced splitting by design introduced by the directional couplers. 2 × 2 multimode interferometers would be a more effective alternative.

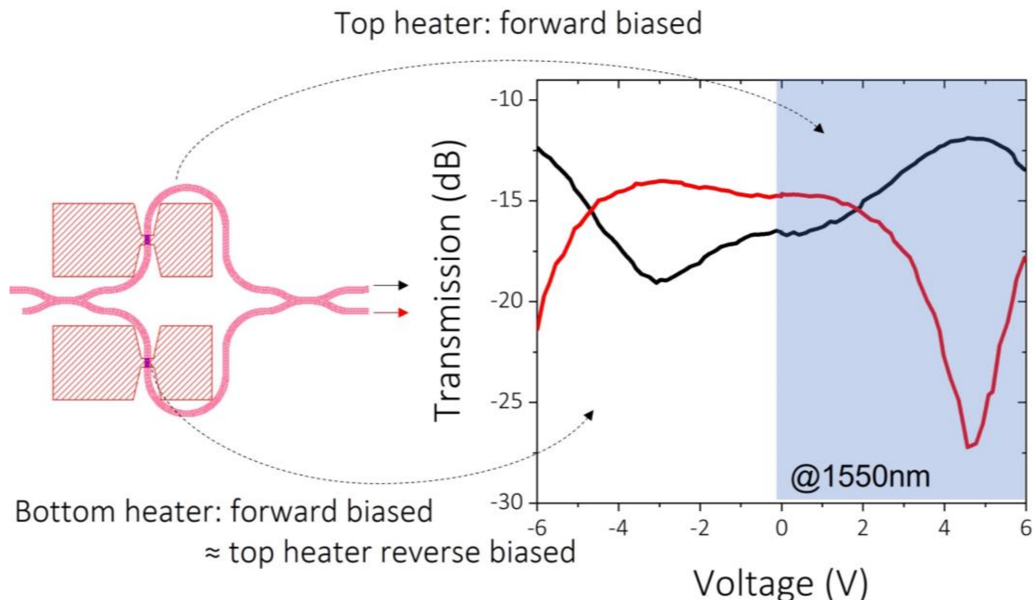

Figure S5. Volatile operation of an MZI switch comprising two crystalline Sb_2Se_3 cells that remain unaltered.

S4. Time-domain measurements

Fig. S6 shows time-domain measurements of an MZI switch at 1565 nm by modulating the two Sb_2Se_3 optical phase shifters with different sequences of amorphization (10.8 V for 400 ns) and crystallization pulses (3.2V varying pulse width between 0.1 and 1 ms). We achieved a 22 dB and 9 dB extinction ratio for each output port with access to intermediate levels and multiple reversible cycles. The stable transmission measurements further demonstrate the nonvolatile nature of our approach.

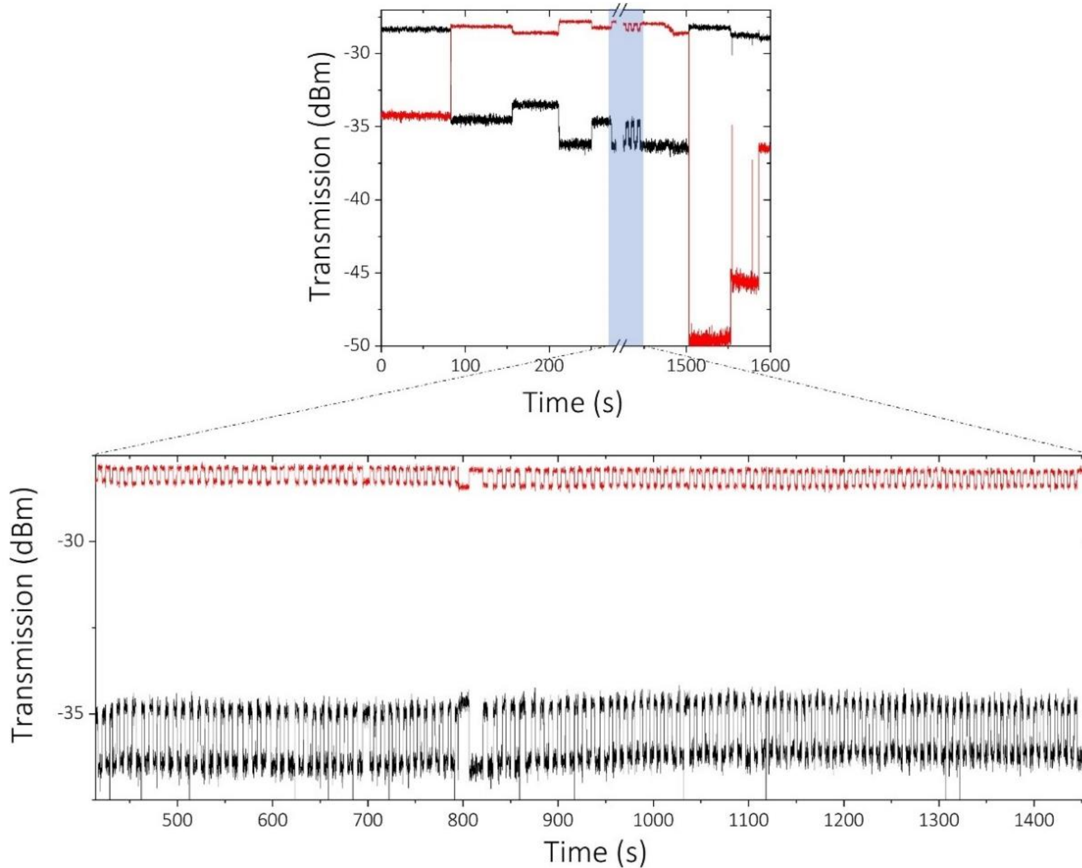

Figure S6. Reversible cycling of a balanced MZI switches a 6μm-long Sb_2Se_3 OPS in each arm. measured in time at $\lambda = 1565$ nm

S5. Propagation loss due to Sb_2Se_3 and doped-silicon

We used microring resonators to estimate the propagation loss of the SOI ridge waveguide alone, with a doped microheater, and with 30nm-thick Sb_2Se_3 cell (including alumina capping) in both amorphous and crystalline states. The results are shown in Fig. S7a, where each dot represents the propagation loss extracted from a single resonance peak. After a Lorentzian fit, we estimated the Q-factor (typically in the 1×10^4 to 3×10^4 range) and the extinction ratio, which we used to calculate the propagation loss for the three cases: critically, under, and over coupled ring. From the results, we concluded that all our ring devices were over coupled, which we expected since by design, with just 150 nm gap, we intended to compensate for the insertion loss (IL) of both the microheater and their Sb_2Se_3 cell; however, their IL was small, and so, the rings remained over coupled. The data in Fig. S7a for the heater and the heater with a Sb_2Se_3 cell in both states was collected using the same device at different fabrication steps. The data for the waveguide with no heater was measured on a reference device on the same chip. The device consisted of a ring of 120 μm in radius and with the microheater shown in Fig. S7c. Although we show here a single device, we achieved

consistent results throughout the same and even different samples – we show an example of the same ring design in a different sample in Fig. S7b.

To estimate the IL due only to the heater, we calculated, from Fig. S7a, $\mathrm{IL}_{heater} = (\alpha_{heater} - \alpha_{No\ heater}) \cdot L = 4\ dB/cm \times 120\ \times 2 \times \pi \times 10^{-4}\ cm =\ 0.301$ dB, and since the microheater was 10 µm long, then the propagation loss through the doped silicon per unit of length was 0.03 dB/µm. Similarly, we calculated the losses after embedding the 6 µm-long Sb_2Se_3 cell shown in Fig. S7c. We found that Sb_2Se_3 in amorphous states has a low IL, undistinguishable from the heater losses under our current analysis. For crystalline Sb_2Se_3, on the other hand, we measured a total insertion loss of 0.21 dB, substracting at least 0.12 dB losses due to scattering effects (see section S6); we conclude that the excess loss upon crystallization of a 6 µm-long Sb_2Se_3 is as low as 0.018 dB/µm. Such an excess loss can be attributed to a non-negligible extinction coefficient in the crystalline state but also to random roughness generated by the volumetric change that PCMs undergo upon switching, which increases losses to scattering. When measuring the devices with five bridges (see Fig. 5 in the main text), the total insertion loss was higher, 0.4 dB, which also accounts for higher scattering given its geometry.

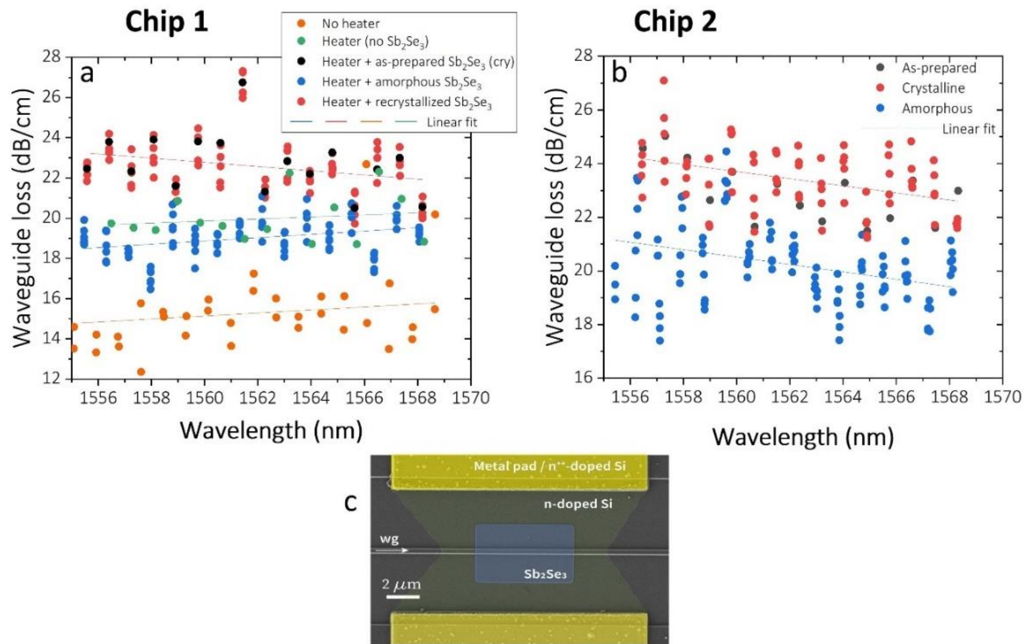

Figure S7. **a.** Waveguide propagation losses for an SOI waveguide with and without heater, and with heater and a Sb_2Se_3 cell in both states. **b.** Waveguide losses for an identical device in a different sample featuring similar results. **c.** Coloured SEM image of the microheater and Sb_2Se_3 cell considered in **a** and **b.**

S6. Scattering losses analysis

We run FDTD simulations to study the scattering losses introduced by the Sb_2Se_3 cell in the near field of a silicon waveguide, taking into account the refractive index shown in Fig. 1. As it has been extensively

studied elsewhere,[4] the insertion loss of embedding a PCM cell onto a photonic waveguide raises from both the material absorption – as studied in the previous S4 section – and scattering effects that imply losing light to the substrate, air, or reflected backwards through the same waveguide. Scattering is particularly strong if the Sb_2Se_3 cell has a flat facet perpendicular to the direction of propagation, just as we have studied in this paper (see Fig. 1 and Fig. S7c). The reasons behind our choice are higher misalignment tolerance and considering a realistic size based on design rules in foundry processes which constrain the area for etching down to the silicon waveguide. A strategy to reduce such losses, at the cost of higher patterning complexity, is patterning the Sb_2Se_3 in shapes that allow an adiabatic coupling between the propagating mode and the material, as demonstrated in Fig. S8.

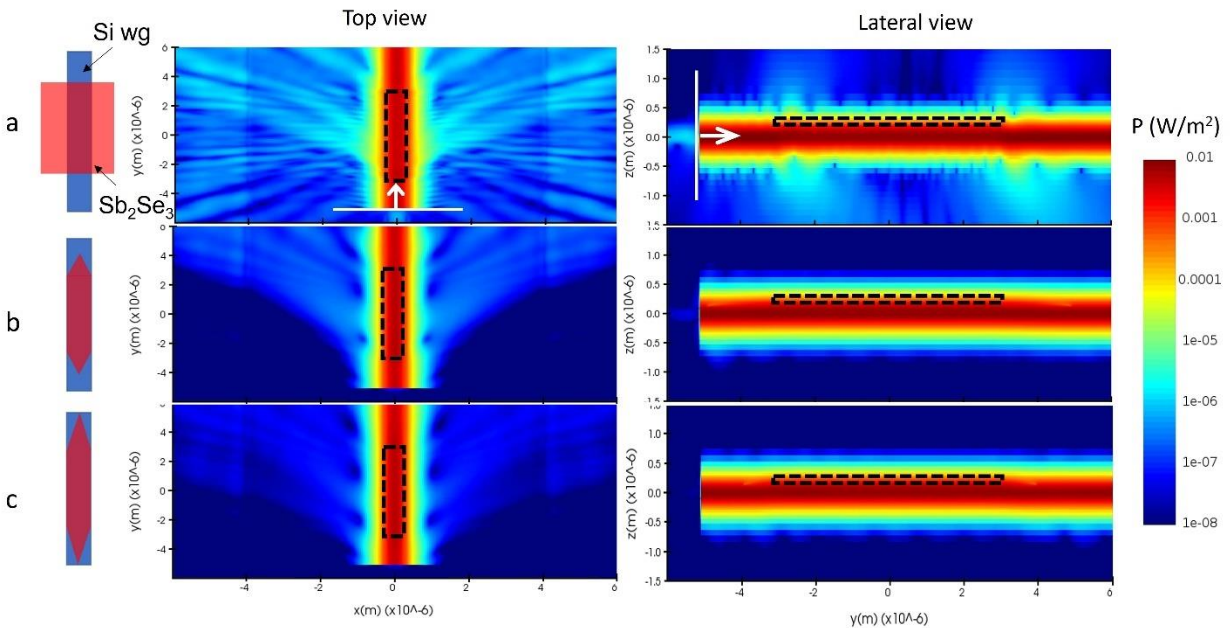

Figure S8. FDTD simulations of the scattering effects due to embedding 30nm-thick crystalline Sb_2Se_3 onto silicon waveguides. Left column corresponds to the geometry under study for each row, the central column corresponds to the top view of the waveguide, and the right column corresponds to the side view. **a** Device studied and measured in this work, corresponding to an alignment-tolerant and foundry compatible square shape with 6 µm in length and 4 µm in width . **b** Tapered Sb_2Se_3 covering only the waveguide (0.5 µm) and with a total length of 8 µm of which 1.5 µm at each end are tapered. **c** same as **b** but with 2.5 µm taper. The dotted lines represent the square part of the PCM cells.

Fig. S9 plots the transmission accounting for both scattering and free-carrier absorption in the doped-silicon region for the three geometries shown in Fig. S8. In the amorphous state, Sb_2Se_3 has a refractive index similar to silicon's, which combined with destructive interference effects for the backscattered light (see Fig. 9d) leads low scattering losses (total ~0.04 dB for the simulated 6 µm-long cell). The total loss when having amorphous Sb_2Se_3 is dominated by the absorption of the doped-silicon microheater, which we demonstrated in our experiments. The heater's IL with amorphous Sb_2Se_3 or without Sb_2Se_3 was identical at 0.3 dB within our experimental error, differing from the simulation yielding 0.15 dB and 0.11 dB, respectively (see Fig. S9c). On the other hand, the simulation results show that the losses are more significant for crystalline Sb_2Se_3 due to more considerable scattering in all directions (see Fig. 8a). Upon

crystallization, the scattering adds 0.12 dB to the insertion loss, which is in the same order of magnitude than the excess loss measured: 0.23 dB (see Section S5).

The results in Fig. S8 and Fig. S9 suggest that the total measured insertion loss of 0.3 dB and 0.5 dB, for microheaters with amorphous and crystalline Sb_2Se_3, respectively, is strongly affected by scattered light and free-carrier absorption in the doped-silicon region. The former can be further decreased by nearly 0.1 dB if a tapered Sb_2Se_3 cell is used. The latter can be reduced by further engineering the microheater to have a lower doping concentration.

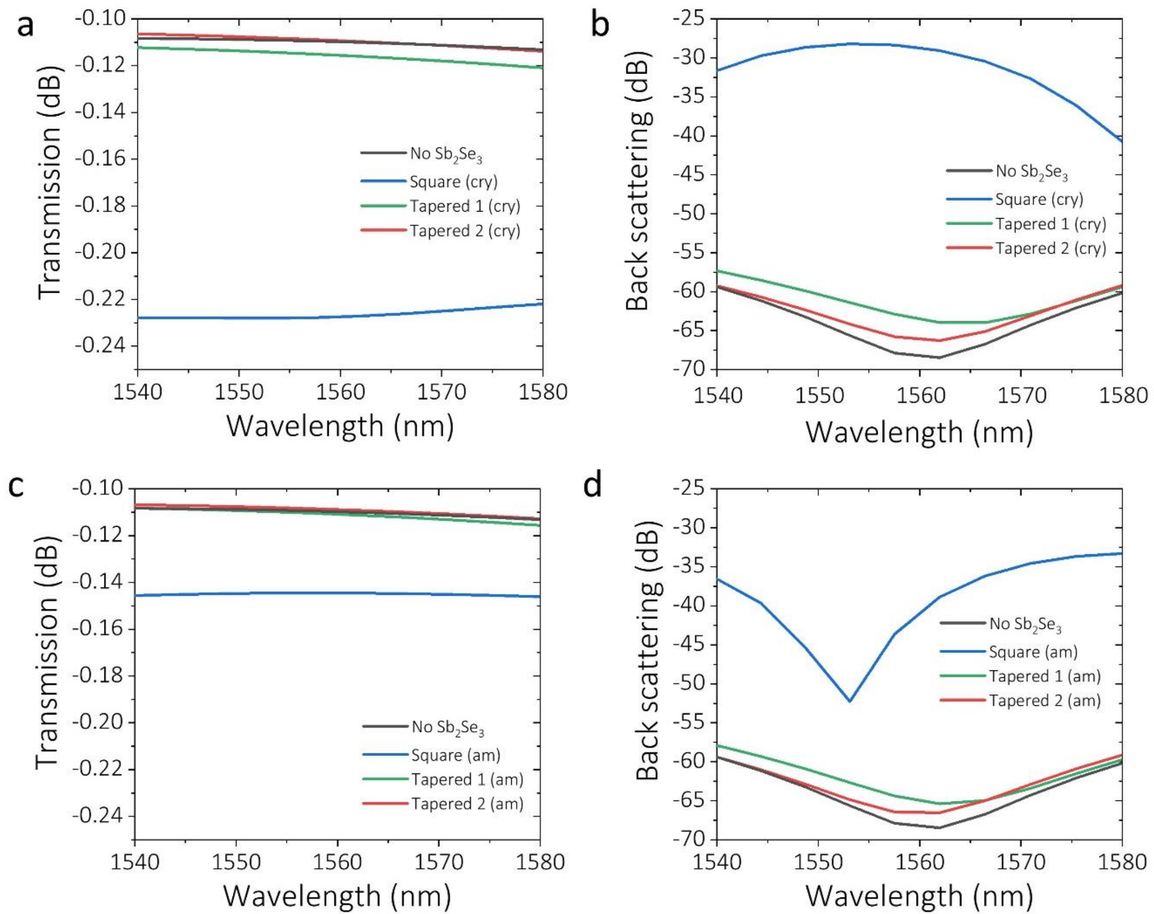

Figure S9. FDTD simulation of the total transmission through the doped-silicon microheater including Sb_2Se_3 cells with the three geometries: square refers to that in Fig. S8a, Tapered 1 to that in Fig. S8b and tapered 2 to Fig. S8c. **a** Transmission for crystalline Sb_2Se_3 cells. **b** Back-scattered light for crystalline Sb_2Se_3 cells. **c** Transmission for amorphous Sb_2Se_3 cells. **d** Back-scattered light for amorphous Sb_2Se_3 cells.

S7. Extinction ratio modulation in add-drop ring resonators

To elucidate the experimental results in the add-drop ring with extinction ratio modulation, we choose the results in Fig. 5c to analyze the coupling coefficients and the modulation upon Sb_2Se_3 switching. To do so, we consider the intensity at the through port, which can be written as:[5]

$$I_{th} = 1 - \frac{(1-\gamma_1)\kappa_1[1-e^{-\alpha L}(1-\gamma_2)(1-\kappa_2)]}{\left[1-\sqrt{(1-\gamma_1)(1-\kappa_1)}\sqrt{(1-\gamma_2)(1-\kappa_2)}e^{-\alpha L/2}\right]^2 + 4\sqrt{(1-\gamma_1)(1-\kappa_1)}\sqrt{(1-\gamma_2)(1-\kappa_2)}e^{-\alpha L/2}\sin^2\frac{\varphi}{2}} \quad (2)$$

where α is the waveguide loss, L is the total length of the ring, and κ_1 and κ_2 are the power coupler coefficients between the ring and the input-through and the add-drop channels, respectively, with a 150 nm gap each. $\kappa = |k|^2$ such that $|t|^2 + |k|^2 = 1$, where t, k are the electric field transmission and coupling coefficients used in the S-matrix formalism.[6]

Similarly, the intensity in the drop port can be written as:

$$I_{drop} = \frac{(1-\gamma_1)(1-\gamma_2)\kappa_1\kappa_2 e^{-\alpha L}}{\left[1-\sqrt{(1-\gamma_1)(1-\kappa_1)}\sqrt{(1-\gamma_2)(1-\kappa_2)}e^{-\alpha L/2}\right]^2 + 4\sqrt{(1-\gamma_1)(1-\kappa_1)}\sqrt{(1-\gamma_2)(1-\kappa_2)}e^{-\alpha L/2}\sin^2\varphi/2} \quad (3)$$

Assuming, as an approximation, that the couplers are lossless, then $\gamma_1, \gamma_2 = 0$. Then,

$$I_{th} = 1 - \frac{\kappa_1[1-e^{-\alpha L}(1-\kappa_2)]}{\left[1-\sqrt{(1-\kappa_1)}\sqrt{(1-\kappa_2)}e^{-\alpha L/2}\right]^2 + 4\sqrt{(1-\kappa_1)}\sqrt{(1-\kappa_2)}e^{-\alpha L/2}\sin^2\frac{\varphi}{2}}\ , \quad (4)$$

and

$$I_{drop} = \frac{\kappa_1\kappa_2 e^{-\alpha L}}{\left[1-\sqrt{(1-\kappa_1)}\sqrt{(1-\kappa_2)}e^{-\alpha L/2}\right]^2 + 4\sqrt{(1-\kappa_1)}\sqrt{(1-\kappa_2)}e^{-\alpha L/2}\sin^2\varphi/2}\ . \quad (5)$$

To find the coefficients κ_1 and κ_2, we solve the systems of equations shown in Eq. (6) and Eq. (7) for a total of six peaks in each of the four experimental spectra: drop and through ports with Sb_2Se_3 in both amorphous and crystalline states. We used a Lorentzian fit to precisely calculate the extinction ratio (ER) and avoid miscalculations due to peak overlapping – especially in the drop port with its low-Q peaks (see Fig. S10a). α_{am} and α_{cry} are taken as the experimental values 19 dB/cm and 22 dB/cm, respectively (see Section S5), and $L = 2\pi \cdot 100\ \mu m$. We used Mathematica 12.0 to solve the equations, and the results, averaged over the six peaks, are also shown in Eq. (6) and Eq. (7).

$$\left.\begin{array}{l} 10\cdot log_{10}\left(\dfrac{I_{drop}(\kappa_1\kappa_{2,am},\alpha_{am},\varphi=0)}{I_{drop}(\kappa_1\kappa_{2,am},\alpha_{am},\varphi=\pi)}\right) = ER_{am,drop} \\ 10\cdot log_{10}\left(\dfrac{I_{th}(\kappa_1\kappa_{2,am},\alpha_{am},\varphi=0)}{I_{th}(\kappa_1\kappa_{2,am},\alpha_{am},\varphi=\pi)}\right) = -ER_{am,through} \end{array}\right\} \begin{array}{l} \{\kappa_1 = 0.647 \pm 0.012; \kappa_{2,am} = 0.541 \pm 0.037\} \\ \{\kappa_1 = 0.640 \pm 0.032; \kappa_{2,am} = 0.562 \pm 0.059\} \end{array} \quad (6)$$

Similarly,

$$\left.\begin{array}{l} 10\cdot log_{10}\left(\dfrac{I_{drop}(\kappa_1\kappa_{2,cry},\alpha_{cry},\varphi=0)}{I_{drop}(\kappa_1\kappa_{2,cry},\alpha_{cry},\varphi=\pi)}\right) = ER_{cry,drop} \\ 10\cdot log_{10}\left(\dfrac{I_{th}(\kappa_1\kappa_{2,cry},\alpha_{cry},\varphi=0)}{I_{th}(\kappa_1\kappa_{2,cry},\alpha_{cry},\varphi=\pi)}\right) = -ER_{cry,through} \end{array}\right\} \begin{array}{l} \{\kappa_1 = 0.666 \pm 0.015; \kappa_{2,cry} = 0.702 \pm 0.019\} \\ \{\kappa_1 = 0.791 \pm 0.023; \kappa_{2,cry} = 0.563 \pm 0.035\} \end{array} \quad (7)$$

Since κ_1 must be the same for both states, we discard the second solution for the crystalline state and take the intersecting interval to conclude that $\kappa_1 = 0.655 \pm 0.004; \kappa_{2,am} = 0.541 \pm 0.037$ and $\kappa_{2,cry} = 0.702 \pm$

0.019. Using the experimentally measured group index $n_g = 3.84$ also extracted from the ring resonators, with excellent agreement across devices and samples, we plot in Fig. S10b the reconstructed spectra with the coupling coefficients used in the calculation, including their minimum and maximum values. In the amorphous state, the minimum and maximum values happened to be in the under- and over coupling regions, meaning that within the range of the solution lies the critical coupling.

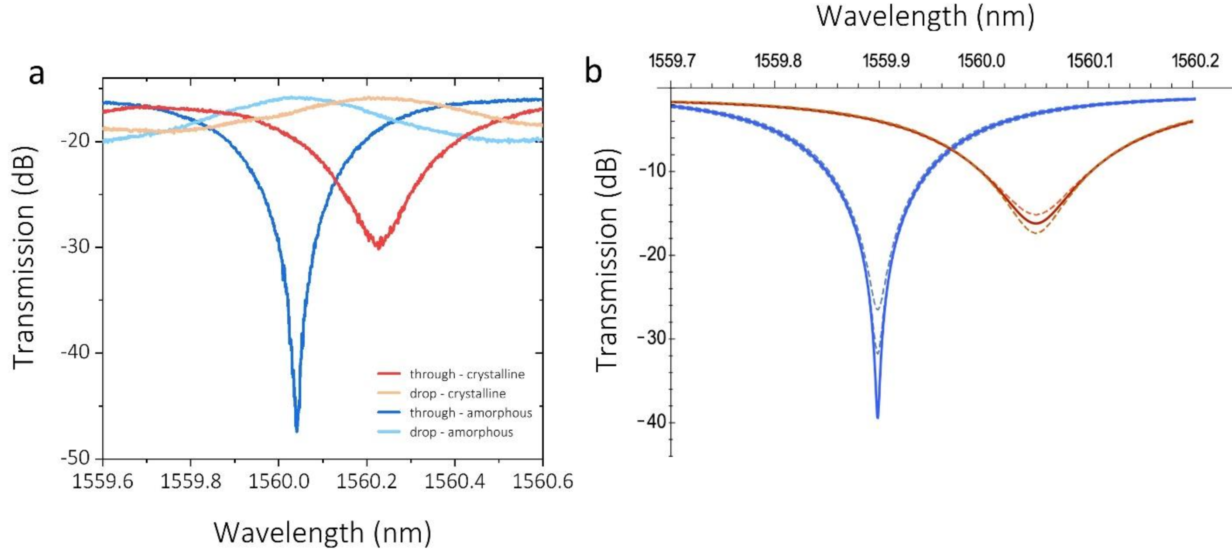

Figure S10. **a**. Experimental data for a single peak in the drop and through ports for Sb_2Se_3 in amorphous and crystalline states. **b**. Reconstructed spectra for the through port with the calculated coupling coefficients. The dotted lines represent the minimum and maximum values for the coupling coefficients $\kappa_{2,am} = 0.541 \pm 0.037$ and $\kappa_{2,cry} = 0.702 \pm 0.019$. In the amorphous state the critical coupling takes place between the minimum and the maximum values.

We used FEM models to study the supermodes in both ring couplers, one without Sb_2Se_3 and the other fully covered with 30nm of Sb_2Se_3, including covering the gap. Fig. S10 shows the results for the four cases and the value of the index difference between odd and even supermodes, Δn, which dictates the strength of the light coupling between both waveguides.[7] Adding Sb_2Se_3 has a significant effect on the coupling coefficient and switching reversibly between amorphous and crystalline Sb_2Se_3 also results, as expected, in modulation of such coupling. In particular, the crystalline state, having a larger Δn, enables more coupling to the secondary waveguide – which we observed experimentally since $\kappa_{2,cry} > \kappa_{2,am}$. In the case of the add-drop ring resonator under study, this situation means that the crystalline state allows more light into the drop port, or equivalently, adds more losses to the light circulating inside the ring resonator. Upon amorphization, the losses inside the ring decrease, and more light goes to the ring-through coupling region, favoring the destructive interference and, therefore, the critical coupling. This can be better understood if considering that critical coupling takes place when:[8]

$$a = \frac{r_1}{r_2} = \frac{\sqrt{1-k_1^2}}{\sqrt{1-k_2^2}} = \frac{\sqrt{1-\kappa_1}}{\sqrt{1-\kappa_2}}, \qquad (8)$$

where $a = e^{-\alpha L}$. For the case of amorphous Sb_2Se_3, and using the experimental value for the propagation loss α_{am}, we have $a = e^{-\alpha_{am} L} = 0.76$. Using Eq. (7), for $\kappa_2 = \kappa_{2,am}$, we have that the attenuation to achieve critical coupling is $a_c = 0.86$. The proximity of these two numbers shows that the amorphous state is close to the critical coupling of the ring resonator. On the other hand, when in the crystalline state, $a = e^{-\alpha_{cry} L} = 0.728$, while the Eq. (7) for $\kappa_2 = \kappa_{2,cry}$ gives $a_c = 1.08$, which is physically impossible to achieve. The crystalline state leads to an over coupled state, and the only way to make the ring operate in the proximity of the critical coupling is by decreasing κ_2, which is exactly what we achieve when switching to amorphous Sb_2Se_3.

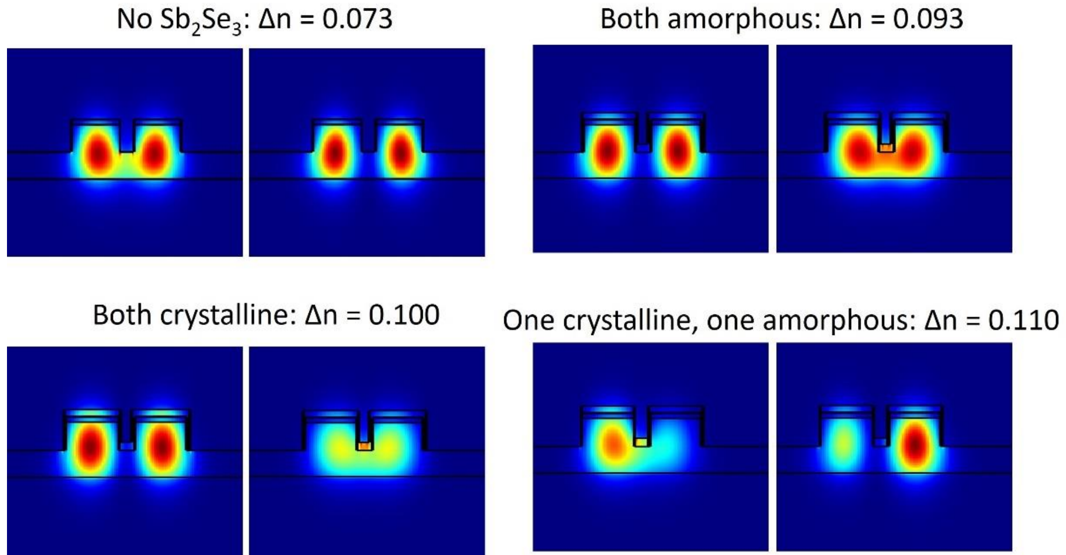

Figure S11. **a**. Simulation of supermodes and calculated difference between the effective refractive index of the odd and even modes.

S8. Other results for MZI modulators

Figure S12a shows a continuous (multi-state) switching by partially crystallizing amorphous Sb_2Se_3 using a 20 µm-long microheater. The continuous switching was achieved by starting with an as-deposited amorphous Sb_2Se_3 cell. Fig. S12b shows the results for an MZI with the four different permutations using a device with 10 µm-long Sb_2Se_3 cells. Extinction ratio over 35 dB is achieved between opposite states with a nearly complete π phase shift modulation. The variations in the ER in both devices are due to the unbalanced directional coupler that splits the output into two different ports (here we show the output for only one of them).

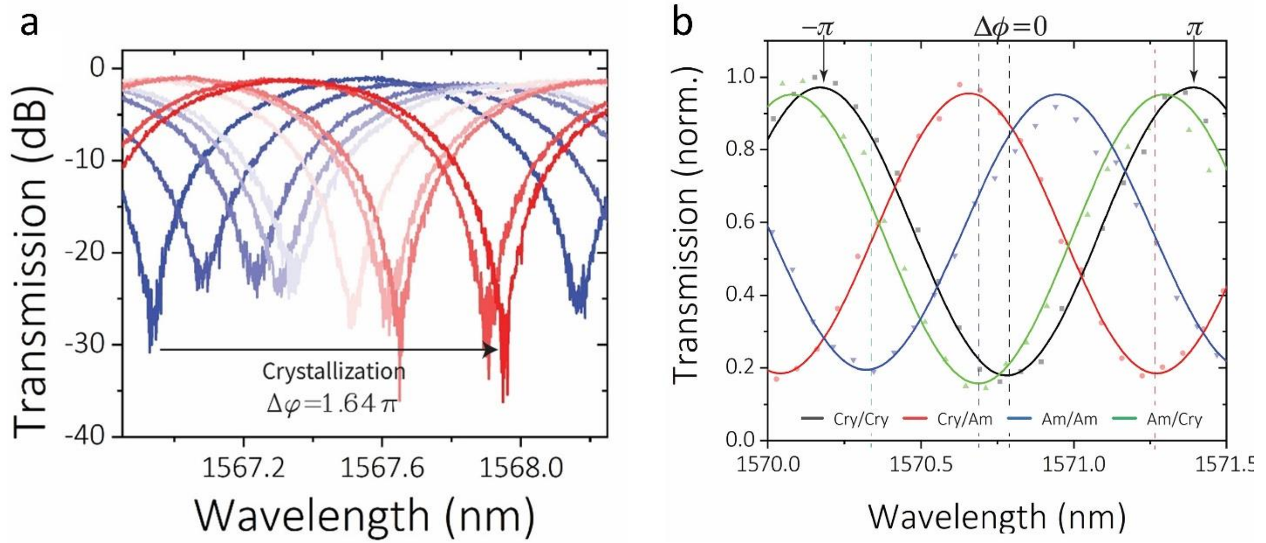

Figure S12. **a** Continuous, multi-state crystallization in as-deposited Sb_2Se_3 . **b** Experimental demonstration of four interferograms corresponding to each phase state permutation in the device shown in a with two 10 µm-long Sb2Se3 on 20 µm-long Sb_2Se_3 cells micorheater OPS. Crystallization was achieved using 6.2 V [3.2V] and 1 ms pulses. Amorphization was achieved with 21 V [10.8 V] and 400 ns pulses.

S9. SEM images for devices after switching

In Fig. S13, we show SEM images of devices after several reversible cycles and after ablation due to voltage pulses heating up beyond the boiling point of the Sb_2Se_3. In particular, the top-left device corresponds to one of the two 'bridges' devices in the MZI measured in Fig. S12b. The bottom-left device corresponds to the microheater in one of the arms of the MZI switch used in Fig. 2d in the main text. The ablated devices show good agreement concerning the simulation since the ablated areas correspond to the expected highest temperature. For the 'bridges' structures, this is particularly important. Even when there is a total of 10 µm of Sb_2Se_3 distributed in five sections of 2 µm each, the maximum we were able to switch is approximated 6 µm corresponding to a total of π phase shift, which we demonstrated in two instances: Fig. 5d in the main text and Fig. S12b. According to our simulations (see Fig. 5a in main text), the heat dissipation in such device leads to a higher temperature in the central bridge that extends laterally toward the extremes. When a pulse is enough to fully amorphize the outer two bridges, the central bridge undergoes a temperature of at least 200 K higher, which causes ablation.

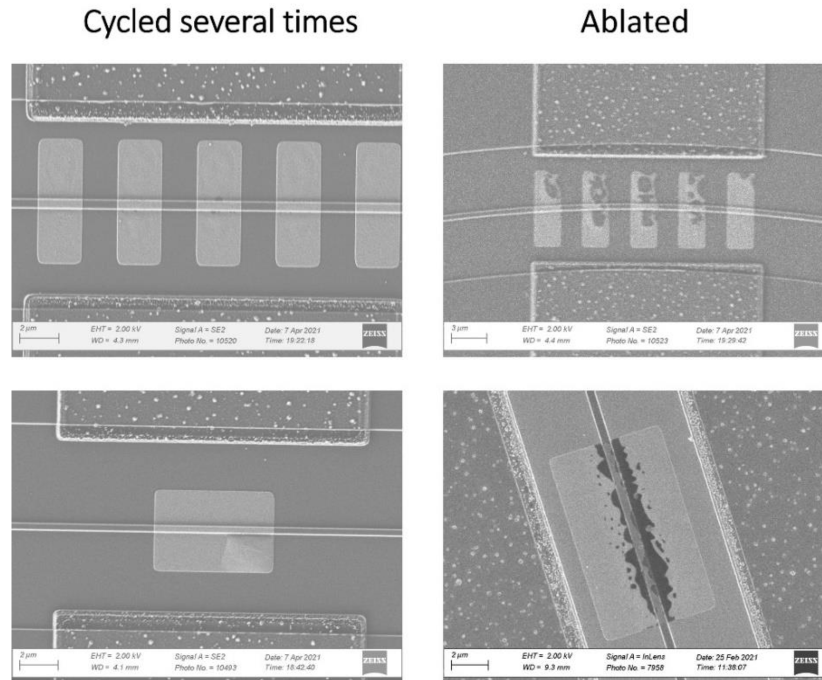

Figure S13. SEM images of devices after cycling reversibly several times and ablated.

S10. References

1. Gosele, U. M. Fast Diffusion in Semiconductors. *Annu. Rev. Mater. Sci.* **18**, 257–282 (1988).

2. Harris, N. C. *et al.* Efficient, compact and low loss thermo-optic phase shifter in silicon. *Opt. Express* **22**, 10487 (2014).

3. Ríos, C. *et al.* Integrated Nonvolatile Phase-shifter Based on Electrically Reconfigurable Low-loss Phase-change Materials. in *Conference on Lasers and Electro-Optics (CLEO)* JTu2P.2 (2021).

4. Rios, C. *et al.* Controlled switching of phase-change materials by evanescent-field coupling in integrated photonics. *Opt. Mater. Express* **8**, 2455–2470 (2018).

5. Bahadoran, M. & Amiri, I. S. Double critical coupled ring resonator-based add–drop filters. *J. Theor. Appl. Phys.* **13**, 213–220 (2019).

6. Yariv, A. Universal relations for coupling of optical power between microresonators and dielectric waveguides. *Electron. Lett.* **36**, 321–322 (2000).

7. Huang, W.-P. Coupled-mode theory for optical waveguides: an overview. *J. Opt. Soc. Am. A* **11**, 963 (1994).

8. Bogaerts, W. *et al.* Silicon microring resonators. *Laser Photonics Rev.* **6**, 47–73 (2012).